








RESEARCH ARTICLE | OCTOBER 14 2025

## Accelerating NMR spectroscopy via parallel SABRE in a continuous-flow system

Jing Yang ; Yen-Tse Cheng; Sören Lehmkuhl ; Juergen J. Brandner ; Mazin Jouda  ;  
Jan G. Korvink  



*Rev. Sci. Instrum.* 96, 105203 (2025)

<https://doi.org/10.1063/5.0285277>



View  
Online



Export  
Citation

### Articles You May Be Interested In

Two-scale structure of the current layer controlled by meandering motion during steady-state collisionless driven reconnection

*Phys. Plasmas* (July 2004)

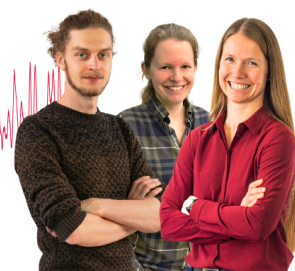
### Webinar From Noise to Knowledge

May 13th – Register now



Zurich  
Instruments

Universität  
Konstanz



# Accelerating NMR spectroscopy via parallel SABRE in a continuous-flow system

Cite as: Rev. Sci. Instrum. 96, 105203 (2025); doi: 10.1063/5.0285277

Submitted: 13 June 2025 • Accepted: 20 September 2025 •

Published Online: 14 October 2025



Jing Yang,<sup>a)</sup> Yen-Tse Cheng, Sören Lehmkuhl,<sup>a)</sup> Juergen J. Brandner,<sup>a)</sup> Mazin Jouda,<sup>b)</sup> and Jan G. Korvink<sup>b)</sup>

## AFFILIATIONS

Karlsruhe Institute of Technology (KIT), Institute of Microstructure Technology (IMT), Eggenstein-Leopoldshafen, 76344, Germany

<sup>a)</sup>Also at: Karlsruhe Nano Micro Facility (KNMF), Hermann-von-Helmholtz-Platz 1, Eggenstein-Leopoldshafen, 76344, Germany

<sup>b)</sup>Authors to whom correspondence should be addressed: [mazin.jouda@kit.edu](mailto:mazin.jouda@kit.edu) and [jan.korvink@kit.edu](mailto:jan.korvink@kit.edu)

## ABSTRACT

Nuclear Magnetic Resonance (NMR) techniques are inherently limited by low thermal polarization, often requiring time-consuming signal averaging to achieve sufficient sensitivity. Parallel detection using multiple decoupled coils improves sample throughput by enabling simultaneous acquisition from multiple samples, partially mitigating these limitations. To further enhance detection sensitivity and acquisition efficiency, we investigated the integration of Signal Amplification By Reversible Exchange (SABRE) hyperpolarization with parallel NMR spectroscopy detection. SABRE significantly increases nuclear spin polarization, allowing high-SNR signal acquisition within a single scan. In this study, hyperpolarized solutions were continuously generated using tube-in-tube reactors and delivered to dual detection coils operated in parallel within a 1.05 T MRI system, enabling simultaneous acquisition of hyperpolarized signals under continuous-flow conditions. Complementary MRI experiments directly demonstrated the sensitivity enhancement achievable with SABRE hyperpolarization, particularly for low-concentration analytes. Building on this, parallel SABRE experiments further validated the feasibility of combining hyperpolarization with simultaneous multi-channel NMR detection to improve measurement efficiency without requiring signal averaging. This work provides an experimental basis for high-throughput NMR detection of low-concentration liquid samples under continuous-flow conditions, with promising potential for applications in metabolic studies and pharmaceutical screening.

© 2025 Author(s). All article content, except where otherwise noted, is licensed under a Creative Commons Attribution (CC BY) license (<https://creativecommons.org/licenses/by/4.0/>). <https://doi.org/10.1063/5.0285277>

## INTRODUCTION

Nuclear Magnetic Resonance (NMR), which encompasses both NMR spectroscopy and magnetic resonance imaging (MRI), is among the most powerful analytical tools, providing detailed insights into molecular structure, dynamics, and interactions.

Due to its non-destructive nature and broad applicability, NMR is widely utilized in chemistry, medicine, and physical sciences. However, a fundamental limitation of conventional NMR techniques is their inherently low sensitivity, which stems from the weak thermal polarization of nuclear spins.

Several strategies have been developed to improve magnetic resonance sensitivity. One approach is to use high-field magnets, which increase nuclear spin polarization and thereby improve the sensitivity of NMR.<sup>1,2</sup> In addition, employing cryoprobes to

cool the RF coil and preamplifier significantly reduces thermal noise in the detection chain, potentially improving the signal-to-noise ratio (SNR) by up to fourfold.<sup>3,4</sup> However, these methods are costly and provide only limited gains in sensitivity. Another approach is the use of microcoils, which enhance mass sensitivity by reducing the detection volume and increasing the filling factor.<sup>5,6</sup> This makes NMR spectroscopy practical for drug screening and metabolic process monitoring, where sample volumes are generally limited.<sup>7</sup>

Despite these advances, when measuring low-concentration samples, the inherently weak polarization necessitates multiple scans to improve the SNR. Consequently, increasing the number of scans significantly extends the experiment duration; for instance, achieving a twofold enhancement in SNR requires quadrupling the number of replicate measurements.

To address this limitation, NMR coil arrays with multiple coils arranged in a synchronized manner have been developed.<sup>8–10</sup> This approach enables simultaneous acquisition from multiple sample regions, leading to an  $n$ -fold reduction in detection time and mitigating the limitations imposed by conventional signal averaging.

An alternative and more efficient approach to overcome the low sensitivity of NMR is hyperpolarization, which breaks the constraints of thermal equilibrium by physical or chemical means. This technique rapidly creates a non-equilibrium spin polarization with an enhanced population difference across energy levels, thereby boosting magnetic resonance sensitivity by several orders of magnitude.<sup>11–13</sup>

Among the commonly used hyperpolarization methods, Dynamic Nuclear Polarization (DNP) transfers electron spin polarization to nuclear spins via microwave-driven dipolar interactions at cryogenic temperatures, requiring both high magnetic fields and low temperatures to achieve efficient polarization. Spin-Exchange Optical Pumping (SEOP) relies on spin-exchange collisions between optically pumped alkali metal atoms and noble gas nuclei (e.g., <sup>129</sup>Xe), thereby transferring polarization from electrons to nuclear spins.<sup>14–16</sup> Theoretically, the DNP can achieve nearly 100% nuclear polarization, while SEOP can attain polarization levels exceeding 50%. Both DNP and SEOP have been applied in clinical practice but require sophisticated instruments and prolonged polarization buildup times.

Parahydrogen Induced Polarization (PHIP) offers a straightforward and low-cost pathway to create significant magnetization on the to-be hyperpolarized (HP) substrates with unsaturated C = C bond via pairwise hydrogenation reaction of parahydrogen (*para*-H<sub>2</sub>) molecules.<sup>17–19</sup> As one of the spin-isomers of the hydrogen molecule, *para*-H<sub>2</sub> is NMR-silent due to its spin order being aligned antiparallel. Generally, the conversion of *para*-H<sub>2</sub> to orthohydrogen (*ortho*-H<sub>2</sub>) is restricted due to the quantum mechanical selection rules. However, through the hydrogenation reaction, the magnetic symmetry of *para*-H<sub>2</sub> is broken. As a consequence, this allows the conversion of the spin order of enriched *para*-H<sub>2</sub> into a large population difference of the two protons at different Zeeman levels, leading to hydrogenated substrates exhibiting enhanced NMR signals.

As a non-hydrogenative variant of PHIP, Signal Amplification By Reversible Exchange (SABRE) rapidly generates substantial polarization of substrates within seconds in the presence of a transient metal-organic catalytic complex in the liquid phase. As illustrated in Fig. 1(a), which shows the schematic representation of the SABRE catalytic complex with an iridium center, the two hydrides from *para*-H<sub>2</sub> and two substrates are bound on the equatorial plane of the SABRE catalytic complex. The monodentate carbene ligand IMes and a substrate are located at the axial positions of the complex. The J-couplings between the two hydrides and the nuclei (here the proton) in the equatorial substrates break the symmetry of *para*-H<sub>2</sub>, and allow for spin order transfer to the bound substrate. Consecutively, the HP substrate dissociates from the metal complex yielding free substrate in solution with magnetic resonance signal enhanced by several orders of magnitude. The vacant site then allows for replenishment with fresh *para*-H<sub>2</sub>, followed by binding of a new to-be-hyperpolarized substrate molecule completing the rehyperpolarization cycle. Hence, SABRE allows for continuous

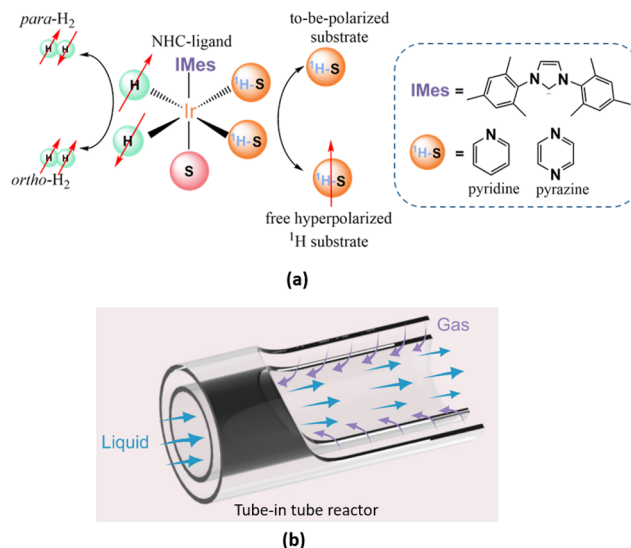


**FIG. 1.** Overview of the SABRE hyperpolarization mechanism and the configuration of the tube-in-tube reactor for SABRE. (a) Schematic representation of SABRE hyperpolarization on a catalytic complex. The spin orders derived from *para*-H<sub>2</sub> are transferred to the substrates (pyridine and pyrazine) on the equatorial plane through the J-coupling network. The hyperpolarized substrates with boosted magnetization dissociate from the catalyst and form free substrates without chemical modification. (b) Sectional view of the tube-in-tube reactor under countercurrent flow conditions.

hyperpolarization as long as the sample is supplied with a fresh *para*-H<sub>2</sub>.<sup>20–22</sup>

The SABRE technique enables the acquisition of a magnetic resonance signal with dramatically enhanced SNR from a single-scan experiment, thereby greatly accelerating the magnetic resonance detection, whether for imaging or spectroscopy. Inspired by the signal-enhancing capabilities of SABRE, we integrated it with parallel NMR spectroscopy<sup>10</sup> to accelerate the detection of the analytes with low-concentration.

In this work, SABRE was implemented under continuous-flow conditions using a tube-in-tube reactor [sectional view in Fig. 1(b)],<sup>23,24</sup> which enabled an efficient gas-liquid contact for polarization transfer. This SABRE platform features a trade-off between polarization buildup and relaxation, both of which are influenced by the flow rate. To describe this flow-dependent trade-off, we first introduce a mathematical model capturing the competing effects of polarization buildup and longitudinal relaxation. We then conducted single-channel NMR spectroscopy measurements across a range of flow rates to identify the optimal flow condition.

Based on the optimal flow rate determined above, we subsequently conducted single-channel MRI measurements to directly compare signal intensities between a fully protonated sample at thermal equilibrium (in the molar concentration range) and a SABRE-hyperpolarized sample at millimolar <sup>1</sup>H concentrations. The results confirmed a substantial enhancement in SNR under hyperpolarized conditions, even with less number of scans and low-concentration, thereby validating SABRE's capability for the rapid detection of dilute analytes.

Consequently, we demonstrate parallel  $^1\text{H}$  SABRE hyperpolarization with dual-channel NMR detection. Two different analyte solutions at millimolar concentrations were hyperpolarized in parallel and delivered to two independent RF coils for simultaneous single-scan NMR spectroscopy. In both channels, the hyperpolarized signals exhibited high SNR ratios from a single scan. Such performance would be unattainable under thermal equilibrium conditions without extensive signal averaging. These results underscore the combined advantages of SABRE hyperpolarization and parallel detection, offering a powerful approach for high-throughput NMR analysis of low-concentration samples.

## METHODS

### System setup

The experimental setup consisted of two main components: a parallel NMR detector and two SABRE polarizers (Fig. 2). The NMR detector was designed to enable the simultaneous acquisition of two NMR spectroscopy signals from separate samples, thereby doubling the throughput and improving the efficiency of NMR detection. The core component of each SABRE platform was a tube-in-tube gas-liquid reactor housed within an electromagnetic coil. The coils generated an optimal magnetic field for efficient polarization transfer via SABRE. The following two subsections provide a detailed description of each component.

### NMR unit cells in parallel

The magnet used in this work is a commercial preclinical MRI system (ICON, Bruker), which supports both NMR spectroscopy and MRI measurements. This system is equipped with a global shim set comprising only three linear shim axes (X, Y, Z), relying on first-order spherical harmonics to correct magnetic field inhomogeneities.

While such first-order shimming is generally sufficient for imaging applications, it imposes limitations on achievable field homogeneity for spectroscopy. Even in single-coil NMR spectroscopy using standard 5 mm tubes, the resulting linewidths typically range from 5 to 10 Hz after careful shimming. When multiple RF coils and samples are introduced, such as in multi-channel or parallel detection setups, the performance of the global shimming further deteriorates, making it challenging to maintain sufficient spectral resolution across spatially separated detection regions.

To overcome these limitations, we utilized a custom-built dual-channel NMR probe installed in the ICON system (Fig. 2). Each detection channel denoted as a NMR cell (NC) consists of an independent RF coil equipped with its own localized shim set (X, Y, Z). By implementing localized shim coils, the conventional isocenter of the magnet was effectively subdivided into multiple, sample-specific isocenters. A key advantage of this design is that it allows independent control of the spherical harmonic shim fields around each coil, enabling flexible and effective compensation for inhomogeneities within the measurement regions, thereby minimizing

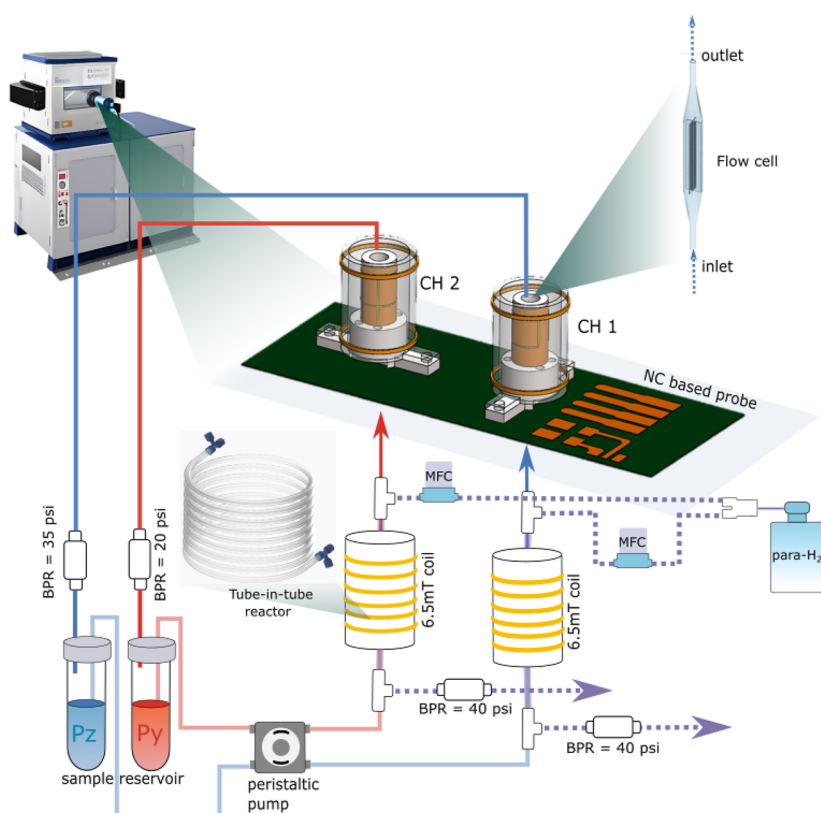


**FIG. 2.** Overview of continuous parallel SABRE experiment setup. The tube-in-tube reactors for continuous SABRE hyperpolarization were wrapped and located inside of the electromagnetic coils with a generated magnetic field of 6.5 mT. The SABRE sample solutions (pyrazine in blue color and pyridine in red color) were continuously hyperpolarized within the tube-in-tube reactors at different pressure differences of the gas and liquid phases. The HP solutions were pumped into the 3D-printed conical-sided flow cells located inside of the RF coils on the NC-based parallel probehead positioned at the 1.05 T horizontal bore magnet.



linewidth broadening due to global shim constraints (details on the design of the NC shim can be found in an earlier publication<sup>8</sup>).

In addition, the  $B_1$  field orientations of the two NCs were deliberately arranged orthogonally to further minimize mutual RF flux interference. The design allows for scalable parallelization while maintaining signal integrity, defined here as the ability to acquire high-quality, undistorted, and decoupled NMR signals from each channel independently.

As illustrated in Fig. 2, both the RF and shim coils were fabricated using flexible printed circuit board (PCB) technology and assembled onto cylindrical 3D-printed polylactic acid (PLA) supports. The sample holder has an inner diameter of 5 mm, while the RF coil is a saddle coil with an optimized 8 mm diameter. The shim coils are positioned around the outer support structure, which has a radius of 8.5 mm. The RF coil geometry follows the design principles outlined by Ginsberg and Melchner,<sup>25</sup> ensuring uniform excitation fields.

### Continuous flow platform for SABRE

The continuous SABRE hyperpolarization platform featured two identical gas–liquid reactors in a tube-in-tube configuration, as shown in Fig. 2. The inlets and outlets of the outer and inner tubings were assembled via two T-junctions (P-713, IDEX Science & Health) and microfluidic tubing fittings (1/4-28 flat-bottom, XP-348 and XP-245, IDEX Science & Health). An extended contacting surface of gas and liquid was provided by 1.5 m overlapping length of the outer and inner tubings.

To achieve efficient polarization of  $^1\text{H}$  via SABRE, the tube-in-tube reactors were coiled and positioned inside two home-made solenoid electromagnetic coils, each providing an optimal magnetic field strength of 6.5 mT for optimal polarization transfer.

The SABRE sample solutions were pumped through the highly gas-permeable inner tubing (Teflon<sup>TM</sup> AF 2400, OD: 0.8 mm, ID: 0.6 mm) using two peristaltic pumps, establishing a counter-flow between the gas and liquid phases. In addition, two back-pressure regulators (IDEX Science & Health, JR-BPR1 and P-791) were installed downstream of the liquid flow in the reactors, maintaining pressures of 35 and 20 psi (1 psi  $\approx$  6.89 kPa) for the pyrazine and the pyridine sample solutions, respectively (Fig. 2).

The *para*- $\text{H}_2$  supply was evenly split into two paths and directed through the outer PTFE tubing (OD: 3.2 mm, ID: 2 mm) of each reactor at a flow rate of 20 ml/min, regulated by a mass flow controller (MFC). Two identical back-pressure regulators with 40 psi cartridges were installed downstream of the gas flow in each reactor. This setup ensured consistent pressure differences  $\Delta p$  between the gas and liquid phases:  $\Delta p = 5$  psi for the reactor for hyperpolarization of pyrazine and  $\Delta p = 20$  psi for the one of pyridine. The positive  $\Delta p$  facilitated the diffusion of *para*- $\text{H}_2$  molecules through the inner tubing wall and into the sample solutions, ensuring efficient mass transfer of *para*- $\text{H}_2$ .

Upon leaving the tube-in-tube reactors, the HP sample solutions were continuously pumped through a PTFE tubing length of 0.35 m (OD: 1.6 mm, ID: 1 mm) and subsequently delivered into the 3D-printed flow cells centered within the RF saddle coils. The flow cell featured with a cylindrical middle section (5 mm in OD) to achieve a high filling factor for the detection coils. The ends of the cell were conically tapered to 2 mm in diameter to

facilitate easy tubing connection, minimize dead volume, and conserve sample solution. The middle section of the flow cell was modified with a cross-shaped phantom for better visualization for MRI detection. After passing through the detection area, the sample solutions were continuously routed to their respective reservoirs, forming a close-loop flow circuit for subsequent regeneration of hyperpolarization.

## EXPERIMENTS AND RESULTS

### Chemical preparation

All SABRE sample solutions were prepared under inert atmosphere using standard Schlenk techniques and high-purity argon (>99.999%) as the inert gas. For SABRE hyperpolarization of  $^1\text{H}$  pyrazine and pyridine, each sample solution contained 3 mmol/l of standard homogeneous SABRE pre-catalyst [IrCl (COD) (IMes)] (IMes = 1,3-bis(2,4,6-trimethylphenyl)imidazol-2-ylidene; COD = cyclooctadiene) and 60 mmol/l of each substrate dissolved in degassed methanol- $d_4$ . The prepared sample solutions were deposited in two Falcon tubes and capped tightly until activation. The pre-catalyst in each sample solution was activated by bubbling fresh *para*- $\text{H}_2$  at a flow rate of 20 ml/min under ambient pressure and room temperature (25 °C) for 10 min.

To obtain *para*- $\text{H}_2$ , normal hydrogen gas (ALPHAGAZ<sup>TM</sup>  $\text{H}_2$ , 99.999%) was continuously supplied with an appropriate flow rate (0.5 l/min), controlled by a mass flow controller. The gas was then passed through a cryostat (cold head) maintained at 23 K and cooled by a commercial water-cooled helium compressor (Advanced Research System, Model ARS-4HW). After contacting the paramagnetic hydrated iron (III) oxide catalyst ( $\text{Fe}_2\text{O}_3 \cdot \text{H}_2\text{O}$ ) in the chamber at the bottom of the cold head, the *para*- $\text{H}_2$  fraction of 98% was generated and collected within an aluminum gas bottle.

### Relationship between magnetization, polarization, and signal intensity

Under thermal equilibrium conditions, the net longitudinal magnetization  $M_0$  of a spin-1/2 nuclear ensemble in a magnetic field  $B_0$  arises from a slight population difference between the Zeeman energy levels,

$$M_0 = \frac{\gamma \hbar}{2} \cdot \Delta n_{\text{thermal}} \quad (1)$$

Here,  $\Delta n_{\text{thermal}} = N_+ - N_-$  is the population difference between the spin-up and spin-down states,  $\gamma$  is the gyromagnetic ratio, and  $\hbar$  is the reduced Planck constant.

The thermal polarization is defined as the fractional population difference,

$$P_{\text{thermal}} = \frac{\Delta n_{\text{thermal}}}{N} \quad (2)$$

Combining Eqs. (1) and (2) gives

$$M_0 = N \cdot \frac{\gamma \hbar}{2} \cdot P_{\text{thermal}} \quad (3)$$

In SABRE technique, the non-equilibrium population difference is generated via the spin order transfer from *para*- $\text{H}_2$ ,

resulting in significantly increased polarization ( $P_{\text{HP}} \gg P_{\text{thermal}}$ ). The corresponding magnetization is

$$M_{\text{HP}} = N \cdot \frac{\gamma \hbar}{2} \cdot P_{\text{HP}}. \quad (4)$$

Thus, the hyperpolarization enhancement factor  $\varepsilon$  is directly given by

$$\varepsilon = \frac{M_{\text{HP}}}{M_0} = \frac{P_{\text{HP}}}{P_{\text{thermal}}}. \quad (5)$$

Although the hyperpolarized magnetization originates from a non-equilibrium state, its temporal decay in a static magnetic field still follows the standard Bloch equation,

$$\frac{dM_z}{dt} = \frac{M_0 - M_z(t)}{T_1}, \quad (6)$$

with its analytical solution,

$$M_z(t) = M_0 + (M_z(0) - M_0)e^{-t/T_1}. \quad (7)$$

Here,  $1/T_1$  is the longitudinal relaxation rate, which is determined by the spin system and its surrounding environment, and is independent of the initial polarization level. Consequently, the relaxation rates of hyperpolarized and thermally polarized magnetizations are governed by the same physical laws.

Finally, the detected NMR signal intensity  $S$  is proportional to the net magnetization  $M_0$  and hence directly to the polarization,

$$S \propto M_0 \propto N \cdot \gamma \cdot P. \quad (8)$$

### Dependence of measured continuous HP signal on flow rate under continuous-flow condition

The hyperpolarization of a substrate in a gas–liquid reactor is critically influenced by the volumetric flow rate and the size of the fluidic circuit. Upon leaving the reactor, the polarization relaxes during transport to the detection volume, and the remaining polarization passes through a detection coil for acquisition.

High volumetric flow rates, which would compensate for the loss of polarization during transport between a reactor and a detection coil, would suffer from a reduced residence time in the reactor, leading to a decreased *para*-H<sub>2</sub> uptake, and consequently, achieves less efficient polarization level. In contrast, lower volumetric flow rates allow to generate more HP substrate in the reactor, while needing longer transfer time to reach the detection coil, which in turn leads to increased polarization loss.

For a better understanding, we incorporate a mathematical model to describe the observed HP signal under continuous flow conditions. The signal is determined by a flow-rate-dependent trade-off between polarization buildup and  $T_1$ -longitudinal relaxation during transport.

In this model, we use the volumetric flow rate  $f$  (unit: ml/min) as the governing parameter to describe the flow-dependent signal behavior. The hyperpolarized signal intensity  $S(f)$  observed at the detector as a function of volumetric flow rate can be expressed as

$$S(f) = S_{\text{max}} \left( 1 - \exp \left( -\frac{t_r(f^\alpha)}{t_b} \right) \right) \cdot \exp \left( -\frac{t_t(f^\beta)}{T_1} \right), \quad (9)$$

where  $S_{\text{max}}$  is the theoretical maximum signal achievable under a static condition,  $t_b$  is the polarization buildup time constant,  $T_1$  is the longitudinal relaxation time,  $f$  is the volumetric flow rate in the unit of ml/min, and  $t_r(f^\alpha) = \frac{L_r \pi r_1^2}{f^\alpha \cdot 60}$  is the effective residence time in the polarization region, scaled by exponent  $\alpha$ .  $L_r = 150$  cm is the overlapping length of inner gas-permeable tubing and the outer tubing of the tube-in tube reactor and  $r_1 = 0.03$  cm is the inner radius of the inner tubing.  $t_t(f^\beta) = \frac{L_t \pi r_2^2}{f^\beta \cdot 60}$  is the effective transport time from the reactor to the detection region, scaled by exponent  $\beta$ .  $L_t = 35$  cm is the distance between the reactor outlet and the detection region and  $r_2 = 0.05$  cm is the inner radius of the transport tubing.

The exponents  $\alpha$  and  $\beta$  are empirical scaling factors that correct for deviations from ideal laminar flow, capturing effects, such as imperfect gas–liquid exchange efficiency and flow dispersion.

It should be noted that one limitation of the model is the simplification of the longitudinal relaxation process using a single effective  $T_1$ . In practice, the sample experiences different magnetic field environments, such as Earth's field during transport toward the magnet and detection field. Therefore, each one is associated with distinct relaxation rates. However, since the primary goal of this modeling is to describe how the flow rate influences the measured HP signal intensity, including the competition between the polarization buildup and relaxation decay, we adopted an effective  $T_1$  to represent the net relaxation effect during sample transfer.

To study the influence of flow rate on the observed HP signal intensity, single-channel NMR spectroscopy of HP pyrazine was conducted at various flow rates using one of the channels of the parallel NMR detector. The HP pyrazine solution was continuously pumped from the tube-in-tube reactor to a 3D-printed cross-shaped flow cell located in the detection area. The pressure difference between the gas and liquid phases in the reactor was maintained at 20 psi throughout the experiment.

As shown by the stacked NMR spectra of HP pyrazine in Fig. 3(a), the signal intensity initially increased and reached a maximum as the flow rate increased from 1 to 6 ml/min [Fig. 3(b)]. Upon further increasing the flow rate, the signal intensity decreased again due to the shorter residence time of the sample in the reactor, which resulted in a less efficient SABRE process. Therefore, the optimal flow rate for generating maximal observed NMR signal intensity is  $f_{\text{opt}} = 6$  ml/min.

As shown in Fig. 3, the mathematical model [Eq. (9)] was fitted to the experimental data as a function of flow rate. The fitted values of  $t_b$ ,  $T_1$ ,  $\alpha$ , and  $\beta$  are 1.15 s, 2.88 s, 2.34, and 0.66.

### SNR enhancement analysis based on MRI comparison

To quantitatively assess the sensitivity enhancement enabled by SABRE hyperpolarization under low-concentration conditions, a comparative MRI study was conducted using thermally polarized methanol and SABRE-hyperpolarized pyrazine solutions. The corresponding proton concentrations were  $c_{\text{H,Ref}} = 98.88$  mol/l for the methanol reference sample (accounting for four protons per methanol molecule) and  $c_{\text{H,HP}} = 0.24$  mol/l for the hyperpolarized pyrazine sample (60 mM pyrazine, four protons per molecule). The reference and HP samples were fed into the detection area under continuous flow conditions at  $f_{\text{opt}} = 6$  ml/min, which was

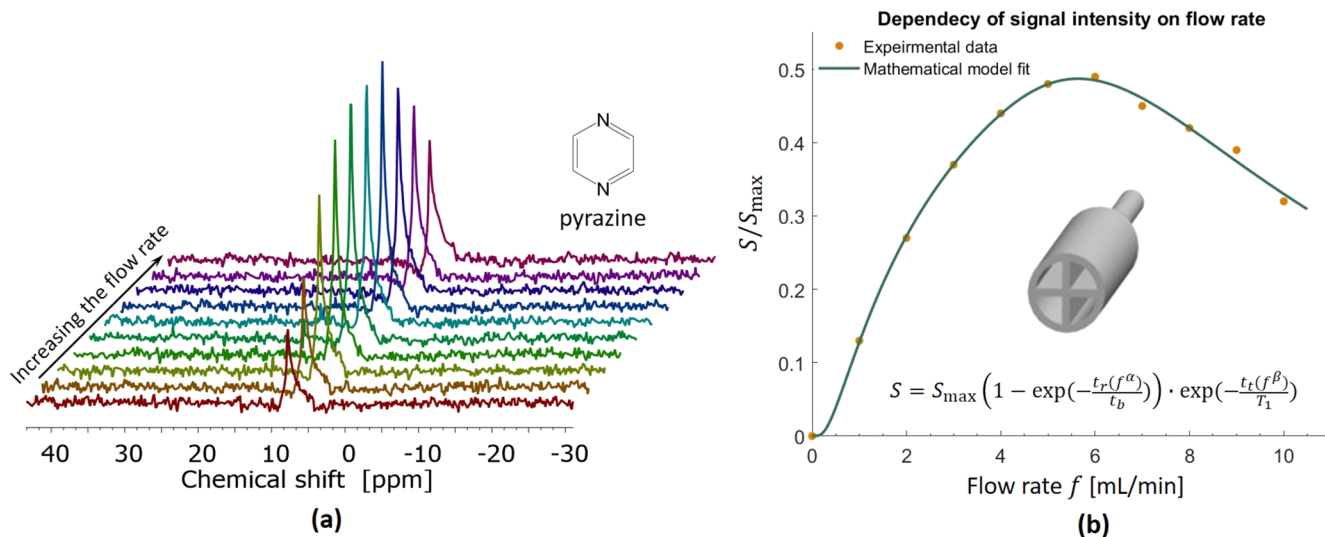


**FIG. 3.** (a) <sup>1</sup>H NMR spectra of HP pyrazine acquired under different volumetric flow rates in the tube-in-tube reactor, with a positive pressure difference of  $\Delta = 20$  psi (137 kPa) between the gas and liquid phases. The sample solution contained 60 mmol/l pyrazine and 3 mmol/l Ir-Imes catalyst dissolved in methanol-d<sub>4</sub>. (b) Dependency of scaled HP signal intensity on flow rate. Orange dots: the experimentally measured signal intensities of the HP pyrazine at different flow rates, scaled to the maximum signal observed under a static condition. Green line: the fitted curve based on the mathematical model [Eq. (9)]. The fitted parameters were:  $t_b = 1.15$  s,  $T_1 = 2.88$  s,  $\alpha = 2.34$ , and  $\beta = 0.66$ . Inset: 3D model of the cross-shaped flow cell used for detection.

determined as the optimal flow rate based on the flow rate vs signal intensity analysis discussed in the preceding section [Fig. 3(b)].

Both the thermally polarized methanol reference and the HP pyrazine sample were imaged on the same 1.05 T MRI system using identical acquisition parameters, including echo time ( $T_E = 7$  ms), repetition time ( $T_R = 80$  ms), matrix size ( $128 \times 128$ ), slice thickness (2.25 mm), flip angle ( $40^\circ$ ), and pixel bandwidth (141.53 Hz/pixel). The only differences were the scan number and the field of view (FOV). The reference image was acquired with  $N_{\text{REF}} = 16$  signal averages and a FOV of  $20 \times 20$  mm<sup>2</sup>, while the hyperpolarized image used  $N_{\text{HP}} = 2$  signal averages and a larger FOV of  $30 \times 30$  mm<sup>2</sup>. To ensure a fair SNR comparison, signal and noise regions of interest (ROIs) were selected such that their corresponding physical areas in both images were matched (Fig. 4).

The SNR of each MR image was determined by manually selecting four signal-dominant regions and four background regions within each MRI dataset (Fig. 4). Circular ROIs of identical physical areas were used to ensure consistent sampling.

For each ROI, the mean pixel intensity was extracted, and the SNR of MR imaging was calculated according to the relation,

$$\text{SNR}_I = \frac{\bar{S}}{\sigma_N}, \quad (10)$$

where  $\bar{S}$  indicates the mean values for the signal and  $\sigma_N$  represents the standard deviation of the background noise, respectively

in Table I. This approach emphasizes the practical detectability of low-concentration signals, which is the primary objective of hyperpolarization-enhanced detection, rather than assessing instrument-limited noise characteristics,

$$\text{SNR}_{I,\text{Ref}} = \frac{696.30}{22.07} \approx 31.6 \quad (11)$$

and

$$\text{SNR}_{I,\text{HP}} = \frac{491.88}{8.39} \approx 58.6. \quad (12)$$

To account for the differences in proton concentration and number of scans, the per-proton normalized sensitivity enhancement factor ( $\epsilon_{1H}$ ) is introduced by

$$\epsilon_{1H} = \frac{\text{SNR}_{I,\text{HP}} \cdot c_{1H,\text{Ref}} \cdot \sqrt{N_{\text{Ref}}}}{\text{SNR}_{\text{Ref}} \cdot c_{1H,\text{HP}} \cdot \sqrt{N_{\text{HP}}}}. \quad (13)$$

Substituting the experimental values yields

$$\epsilon_{1H} = \frac{58.6 \times 98.88 \times \sqrt{16}}{31.6 \times 0.24 \times \sqrt{2}} \approx 2161. \quad (14)$$

This calculation result demonstrates that after normalizing for the proton concentration and number of scans, SABRE

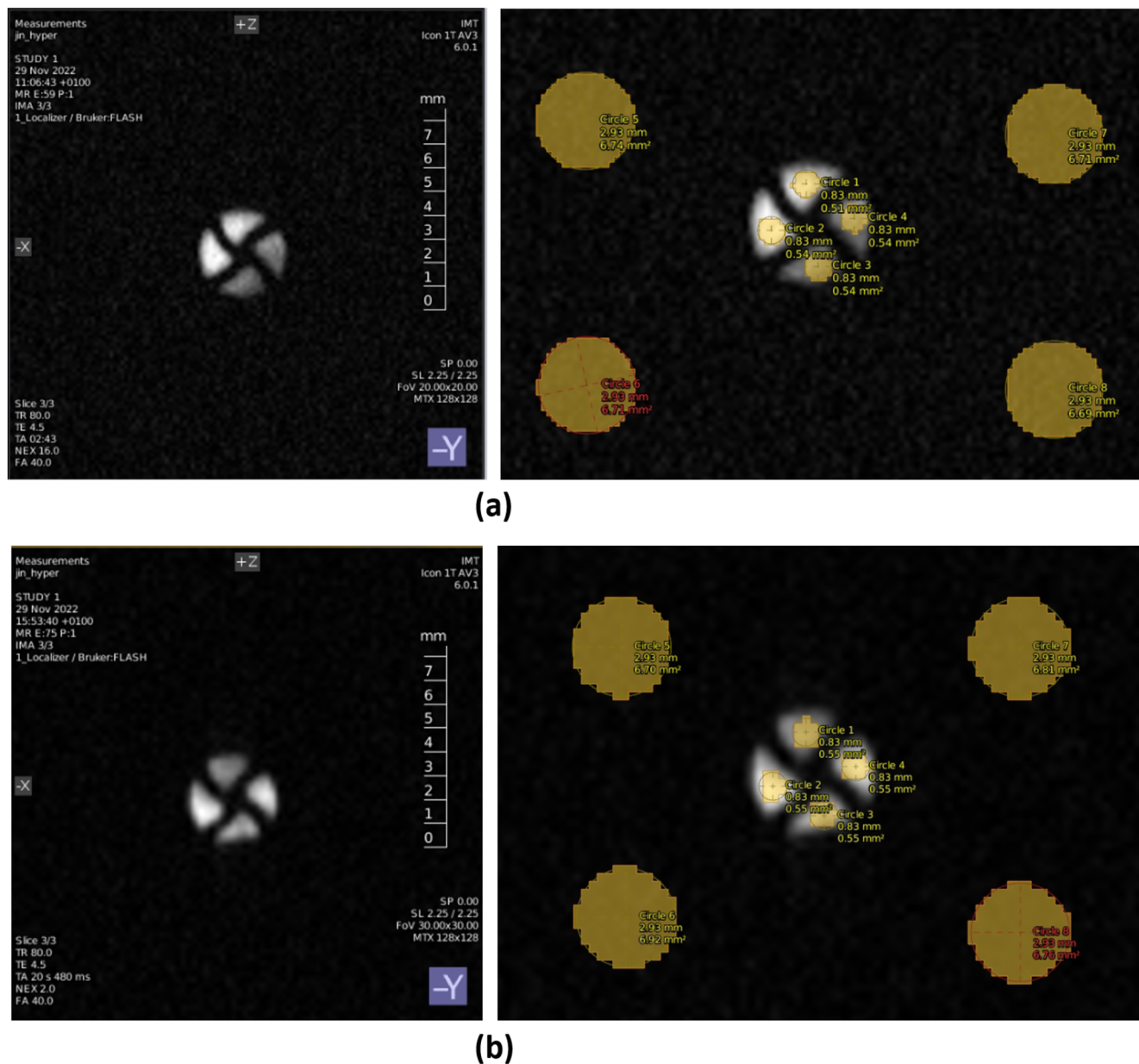


**FIG. 4.** MR images and corresponding ROI selections for SNR analysis under continuous flow conditions at a flow rate of 6 ml/min. (a) Thermally polarized methanol reference sample ( $c_{\text{H}} = 98.88$  mol/l, 16 scans). (b) SABRE HP pyrazine sample ( $c_{\text{H}} = 0.24$  mol/l, 2 scans). Left column: Original MRI images acquired using identical imaging parameters. Right column: ROI selections for SNR calculation, where central small ROIs represent signal-dominant regions and peripheral ROIs represent background noise regions.

hyperpolarization provides approximately a 2161-fold improvement in detection sensitivity per proton compared to thermal equilibrium conditions. Such an enhancement demonstrates the particular suitability of SABRE hyperpolarization for the detection of metabolites and biochemical intermediates that typically exist from nano- to millimolar concentrations in biological systems. In these scenarios, conventional NMR spectroscopy and MRI methods

are often inadequate due to insufficient sensitivity and prohibitively long acquisition times.

### Parallel SABRE hyperpolarization of pyrazine and pyridine

Parallel  $^1\text{H}$  SABRE hyperpolarization of pyrazine and pyridine was conducted with simultaneous NMR detection in two parallel



**TABLE I.** Comparison of mean signal and standard deviation of background noise levels for a reference sample (methanol) and hyperpolarized pyrazine under different proton concentrations and scan numbers.

		Reference	HP
		(Methanol, $c_{\text{H,Ref}} = 98.88 \text{ M}$ , 16 scans)	(Pyrazine, $c_{\text{H,HP}} = 0.24 \text{ M}$ , 2 scans)
Signal region (mean value, $\bar{S}$ )	1	217.00	85.18
	2	246.70	159.50
	3	102.90	104.20
	4	129.70	143.00
Background region (std Dev, $\sigma_N$ )	5	5.50	1.99
	6	5.43	2.29
	7	5.42	2.18
	8	5.72	1.93

channels using the dual RF coils on the NC-based probe. After hyperpolarization in the two tube-in-tube gas-liquid reactors, the HP pyrazine and pyridine were continuously fed into parallel RF coils (CH 1 and CH 2), at an optimized flow rate of 6 ml/min, as determined from preliminary experiments [Fig. 3(b)].

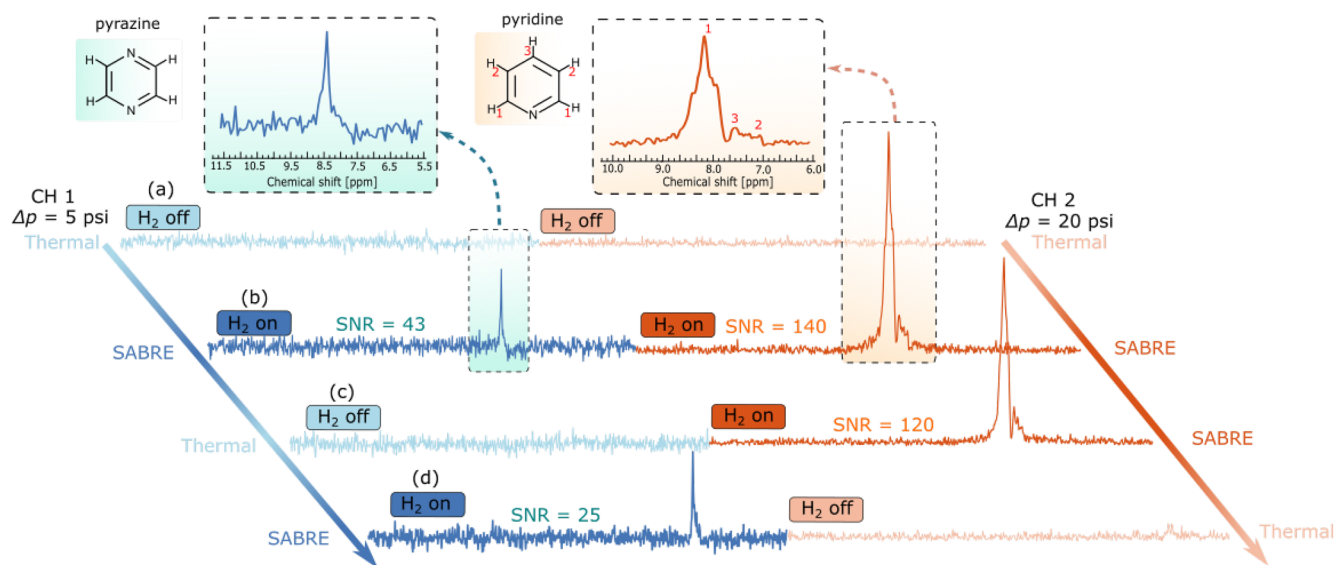
One RF coil was connected to the ICON MRI system for a standard  $^1\text{H}$  single-pulse experiment using the ParaVision software interface (version 6.0.1, Bruker), while the second coil was connected to a separate NMR spectrometer system (Kea2, Magritek). A transistor-transistor logic (TTL) line connected the two systems

to ensure precise synchronization of RF pulse excitation and signal acquisition, enabling truly parallel data collection from both hyperpolarized samples.

Four sets of experiments were conducted to simultaneously acquire signals from the samples fed into the flow cells in CH 1 and CH 2. The results are presented as stacked spectra in Fig. 5. In the initial set of experiments, the supply of *para*- $\text{H}_2$  was turned off in the gas pathways of both tube-in-tube reactors to measure the thermal equilibrium signals of pyrazine and pyridine. However, due to the low millimolar-range concentrations in the single-scan experiments, the peaks in the recorded spectra were barely discernible [Fig. 5(a)].

In the second set of experiments, *para*- $\text{H}_2$  delivery was then commenced to both reactors, which initiated the hyperpolarization of substrates via SABRE. After 60 s of *para*- $\text{H}_2$  exposure, NMR signals from both channels were acquired simultaneously within a single scan. Notably, a distinct singlet peak at 8.5 ppm with an amplitude-based SNR of 43 was observed in the pyrazine spectrum, while peaks between 7.0 and 8.6 ppm were resolved in the pyridine spectrum.

The full width at half maximum (FWHM) of the hyperpolarized pyrazine peak was measured to be  $\sim 0.6 \text{ ppm}$  (27 Hz at 1.05 T). This relatively broad linewidth arises from two main factors: (i) the limited shimming capability of both the global shimming coils and the localized shim coils integrated into the custom NC probe, which are restricted to first-order corrections, and (ii) the cylindrical flow cell with an internal cross-shaped structure, which introduces geometric-induced magnetic field inhomogeneities. Together, these factors contribute to reduced field homogeneity in the detection region. Consequently, the expected triplet splitting of pyridine in the NMR spectrum was not fully resolved. Instead, the signals from the protons at the *para*- and *meta*-positions coalesced into a broader

**FIG. 5.** Parallel  $^1\text{H}$  spectra of pyrazine and pyridine, acquired under SABRE hyperpolarization or thermal equilibrium conditions. The sample solutions were continuously flowing from the tube-in-tube gas-liquid reactors under different *para*- $\text{H}_2$  supply conditions:  $\Delta p = 5 \text{ psi}$  in channel 1 for pyrazine (CH 1) and  $\Delta p = 20 \text{ psi}$  in channel 2 for pyridine (CH 2). (a) CH 1: *para*- $\text{H}_2$  off, CH 2: *para*- $\text{H}_2$  off; (b) CH 1: *para*- $\text{H}_2$  on, CH 2: *para*- $\text{H}_2$  on; (c) CH 1: *para*- $\text{H}_2$  off, CH 2: *para*- $\text{H}_2$  on; and (d) CH 1: *para*- $\text{H}_2$  on, CH 2: *para*- $\text{H}_2$  off.



peak, resulting in an apparent doublet-like pattern. The most intense peak, originating from the ortho-proton, exhibited an SNR of 140 [Fig. 5(b)]. The higher SNR value of the pyridine peak, compared to that of pyrazine, resulted from the greater pressure difference ( $\Delta p = 20$  psi) applied to the tube-in-tube reactor for hyperpolarizing the pyridine sample solution, relative to that used ( $\Delta p = 5$  psi) for the pyrazine sample.

Subsequently, the *para*-H<sub>2</sub> supply in CH 1 was discontinued, while it remained constant in CH 2. The absence of *para*-H<sub>2</sub> caused the pyridine sample in CH 1 to revert to its thermal equilibrium state, rendering it undetectable with a single scan. In contrast, CH 2 still contained hyperpolarized pyrazine solution, which produced a sufficiently strong signal to be observed with an SNR of 120 [Fig. 5(c)].

In the fourth set of experiments, the *para*-H<sub>2</sub> supply was reactivated in CH 1 and turned off in CH 2, resulting in rehyperpolarization of pyrazine and relaxation of the HP pyridine to its thermal equilibrium state. However, the signal intensity of hyperpolarized pyridine was weaker than in the second set of experiments, possibly due to magnetic field drift of the non cryocooled MRI system. Such drift may shift the Larmor frequency away from the initially tuned frequency of the RF coil, leading to suboptimal resonance conditions and reduced SNR. Meanwhile, in the CH 2 spectrum, the thermally equilibrated pyridine resonance was too weak to be detected [Fig. 5(d)].

The experimental results demonstrated that, following the SABRE hyperpolarization, the main peak of each HP substrate became discernible from a single scan—an outcome that was unattainable under thermal equilibrium conditions with the parallel coils and samples at such low concentrations. While both pyrazine and pyridine samples were hyperpolarized and detected simultaneously in each channel, no signal interference or crosstalk was observed between the parallel RF coils, which is attributed to their orthogonal geometric configuration.

While the absence of crosstalk demonstrates the reliability of parallel detection, the marked signal enhancement provided by hyperpolarization is particularly valuable for low-concentration samples, where thermal signals typically fall below the single-scan detection threshold and require signal averaging over many scans to become observable.

Under our experimental conditions, including low-concentration samples and suboptimal magnetic field homogeneity due to first-order shimming, the thermal signal was not detectable in a single scan due to the intrinsically low thermal polarization and limited detection sensitivity. Therefore, we conservatively set the single-scan SNR of the thermal signal to  $\text{SNR}_{\text{thermal}} = 1$  for comparison purposes.

In contrast, hyperpolarized pyrazine and pyridine yielded the amplitude based-SNRs of 43 and 140 [Fig. 5(b)]. This implies that  $\sim 43^2 = 1,849$  and  $140^2 = 19,600$  scans, would be required under thermal equilibrium conditions to achieve equivalent SNRs, given that the SNR increases with the square root of the number of scans.

Therefore, it demonstrates that SABRE hyperpolarization can effectively reduce the acquisition time by several orders of magnitude. When combined with a parallel coil array, the measurement throughput is further increased, enabling simultaneous acquisition of multiple hyperpolarized samples. This dual approach not only accelerates data collection but also extends the applicability of

high-throughput NMR to analytes present at concentrations previously undetectable by conventional methods.

## CONCLUSION

In this work, we developed a continuous-flow SABRE hyperpolarization setup integrated with parallel NMR detection, enabling simultaneous acquisition of hyperpolarized signals from low-concentration liquid samples. Despite these advantages, the current system has several limitations: it is restricted to <sup>1</sup>H detection, simultaneous MRI is not feasible due to the shared global gradient, and the achievable spectral resolution is limited by first-order shimming.

To expand the nuclear detection range, future implementations could integrate multinuclear capabilities (e.g., <sup>13</sup>C, <sup>19</sup>F, and <sup>15</sup>N) into the parallel probe design. This would extend the platform's utility to a broader set of hyperpolarized targets and metabolic flux analysis.<sup>26,27</sup>

For MRI functionality, enabling simultaneous imaging across multiple channels would require improvements, such as localized gradient coils<sup>28</sup> or RF encoding techniques.<sup>29</sup> These developments could open the door to spatially resolved, parallel imaging of hyperpolarized substrates.

Improving spectral resolution will require enhanced magnetic field homogeneity. Incorporating higher-order shim coils<sup>30</sup> or adaptive shimming strategies, such as AI-assisted shimming,<sup>31</sup> would help resolve fine spectral features, thereby facilitating applications in chiral discrimination<sup>32,33</sup> and drug screening.<sup>34</sup>

In summary, the parallel SABRE platform demonstrates its capability for the rapid characterization of low-concentration samples. With continued technical refinements, it holds strong potential to enable multinuclear, high-throughput, and high-sensitivity NMR analysis.

## ACKNOWLEDGMENTS

J.Y. and J.B. acknowledge financial support from the German Research Foundation (DFG) under the Grant Agreement No. BR 4175/5-1. M.J. and J.G.K. acknowledge financial support from the DFG via Grant No. CRC 1527 (*HyperION*). M.J. additionally acknowledges the financial support from the DFG via Grant No. CRC SFB-1537 *ECOSENSE*. J.G.K. acknowledges financial support from the European Union via the ERC Synergy Grant No. 951459 (*HiSCORE*). Support from the Karlsruhe Nano Micro Facility KNMF is also gratefully acknowledged.

## AUTHOR DECLARATIONS

### Conflict of Interest

The authors have no conflicts to disclose.

### Author Contributions

J.Y. and Y.-T.C. contributed equally to this work.

Conceptualization was performed by J.Y., Y.C., M.J., and J.G.K. J.Y. and Y.C. helped in writing of the original draft. Construction of the

setup and experiments was done by J.Y. and Y.C. J.Y., Y.C., and S.L. helped in result analysis. Funding acquisition was done by M.J., J.J.B., and J.G.K.. All authors have reviewed, edited, and agreed to the published version of the manuscript.

**Jing Yang:** Conceptualization (lead); Data curation (lead); Formal analysis (lead); Investigation (lead); Methodology (lead); Software (lead); Validation (lead); Visualization (lead); Writing – original draft (lead); Writing – review & editing (lead). **Yen-Tse Cheng:** Conceptualization (lead); Data curation (lead); Formal analysis (lead); Investigation (lead); Methodology (lead); Software (lead); Validation (lead); Visualization (lead); Writing – original draft (equal); Writing – review & editing (equal). **Sören Lehmkuhl:** Formal analysis (equal); Validation (equal); Writing – review & editing (equal). **Juergen J. Brandner:** Funding acquisition (equal); Project administration (equal); Resources (equal); Supervision (equal); Writing – review & editing (equal). **Mazin Jouda:** Conceptualization (equal); Data curation (equal); Formal analysis (equal); Funding acquisition (equal); Methodology (equal); Resources (equal); Software (equal); Supervision (equal); Validation (equal); Visualization (equal); Writing – review & editing (equal). **Jan G. Korvink:** Conceptualization (equal); Formal analysis (equal); Funding acquisition (equal); Methodology (equal); Project administration (equal); Supervision (equal); Validation (equal); Writing – review & editing (equal).

## DATA AVAILABILITY

The data that support the findings of this study are available from the corresponding authors upon reasonable request.

## REFERENCES

- <sup>1</sup>E. Moser, E. Laistler, F. Schmitt, and G. Kontaxis, *Front. Phys.* **5**, 33 (2017).
- <sup>2</sup>K. Uğurbil, G. Adriany, P. Andersen, W. Chen, M. Garwood, R. Gruetter, P.-G. Henry, S.-G. Kim, H. Lieu, I. Tkac *et al.*, *Magn. Reson. Imaging* **21**, 1263 (2003).
- <sup>3</sup>H. Kovacs, D. Moskau, and M. Spraul, *Prog. Nucl. Magn. Reson. Spectrosc.* **46**, 131 (2005).
- <sup>4</sup>D. Moskau, H. Kovacs, R. Kümmerle, K. Colson, G. Collier, and M. W. Ger-  
mann, *New CryoProbe™ Models for Diverse Analytical Challenges*, 157 (Bruker  
Spin Rep, 2006), p. 35.
- <sup>5</sup>J. G. Korvink, N. MacKinnon, V. Badilita, and M. Jouda, *J. Magn. Reson.* **306**,  
112 (2019).
- <sup>6</sup>S. S. Zaleskiy, E. Danieli, B. Blumich, and V. P. Ananikov, *Chem. Rev.* **114**, 5641  
(2014).
- <sup>7</sup>C. Fernández and W. Jahnke, *Drug Discovery Today: Technol.* **1**, 277 (2004).
- <sup>8</sup>Y.-T. Cheng, M. Jouda, and J. Korvink, *Sci. Rep.* **12**, 14149 (2022).
- <sup>9</sup>K.-M. Lei, D. Ha, Y.-Q. Song, R. M. Westervelt, R. Martins, P.-I. Mak, and D.  
Ham, *Anal. Chem.* **92**, 2112 (2020).
- <sup>10</sup>Ě. KupčeKupče, A. G. Webb, J. R. J. Yong, T. D. W. Claridge, and T. D. Claridge,  
*Nat. Rev. Methods Primers* **1**, 27 (2021).
- <sup>11</sup>J. Eills, D. Budker, S. Cavagnero, E. Y. Chekmenev, S. J. Elliott, S. Jannin, A.  
Lesage, J. Matysik, T. Meersmann, T. Prisner *et al.*, *Chem. Rev.* **123**, 1417 (2023).
- <sup>12</sup>K. V. Kovtunov, E. V. Pokochueva, O. G. Salnikov, S. F. Cousin, D. Kurzbach,  
B. Vuichoud, S. Jannin, E. Y. Chekmenev, B. M. Goodson, D. A. Barskiy, and I. V.  
Koptug, *Chem.—Asian J.* **13**, 1857 (2018).
- <sup>13</sup>M. E. Halse, *Trends Anal. Chem.* **83**, 76 (2016).
- <sup>14</sup>A. C. Pinon, A. Capozzi, and J. H. Ardenkjær-Larsen, *Magn. Reson. Mater.  
Phys., Biol. Med.* **34**, 5 (2021).
- <sup>15</sup>J. H. Ardenkjær-Larsen, *J. Magn. Reson.* **264**, 3 (2016).
- <sup>16</sup>A. S. Khan, R. L. Harvey, J. R. Birchall, R. K. Irwin, P. Nikolaou, G. Schrank, K.  
Emami, A. Dummer, M. J. Barlow, B. M. Goodson, and E. Y. Chekmenev, *Angew.  
Chem., Int. Ed.* **60**, 22126 (2021).
- <sup>17</sup>C. R. Bowers and D. P. Weitekamp, *Phys. Rev. Lett.* **57**, 2645 (1986).
- <sup>18</sup>C. R. Bowers and D. P. Weitekamp, *J. Am. Chem. Soc.* **109**, 5541 (1987).
- <sup>19</sup>S. Glöggler, J. Colell, and S. Appelt, *J. Magn. Reson.* **235**, 130 (2013).
- <sup>20</sup>P. J. Rayner and S. B. Duckett, *Angew. Chem., Int. Ed.* **57**, 6742 (2018).
- <sup>21</sup>N. Eshuis, N. Hermkens, B. J. A. van Weerdenburg, M. C. Feiters, F. P. J. T.  
Rutjes, S. S. Wijmenga, and M. Tessari, *J. Am. Chem. Soc.* **136**, 2695 (2014).
- <sup>22</sup>J. Yang, R. Xin, S. Lehmkuhl, J. G. Korvink, and J. J. Brandner, *Sci. Rep.* **14**,  
21022 (2024).
- <sup>23</sup>S. Lehmkuhl, M. Wiese, L. Schubert, M. Held, M. Küppers, M. Wessling, and B.  
Blümich, *J. Magn. Reson.* **291**, 8 (2018).
- <sup>24</sup>P. M. TomHon, S. Han, S. Lehmkuhl, S. Appelt, E. Y. Chekmenev, M.  
Abolhasani, and T. Theis, *ChemPhysChem* **22**, 2526 (2021).
- <sup>25</sup>D. M. Ginsberg and M. J. Melchner, *Rev. Sci. Instrum.* **41**, 122 (1970).
- <sup>26</sup>A. P. Teixeira, S. S. Santos, N. Carinhas, R. Oliveira, and P. M. Alves,  
*Neurochem. Int.* **52**, 478 (2008).
- <sup>27</sup>W. van Winden, D. Schipper, P. Verheijen, and J. Heijnen, *Metab. Eng.* **3**, 322  
(2001).
- <sup>28</sup>F.-H. Lin, T. Witzel, G. Schultz, D. Gallican, W.-J. Kuo, F.-N. Wang, J. Hennig,  
M. Zaitsev, and J. W. Belliveau, *Magn. Reson. Med.* **68**, 1145 (2012).
- <sup>29</sup>K. Selvaganesan, Y. Ha, H. Sun, Z. Zhang, C. Sun, A. Samardzija, G. Galiana,  
and R. T. Constable, *Sci. Rep.* **14**, 3307 (2024).
- <sup>30</sup>Z. Lin, Z. Zhang, J. Li, Z. Gao, Z. Chu, Y. Liu, P. Zhang, L. Wu, and C. Zhou,  
*Med. Phys.* **52**, 3270 (2025).
- <sup>31</sup>M. Becker, Y.-T. Cheng, A. Voigt, A. Chenakkara, M. He, S. Lehmkuhl, M.  
Jouda, and J. G. Korvink, *Sci. Rep.* **13**, 17983 (2023).
- <sup>32</sup>P. Lazzeretti, *J. Phys.: Condens. Matter* **29**, 443001 (2017).
- <sup>33</sup>S. Wadhwa, D. Buyens, and J. G. Korvink, *Adv. Mater.* **36**, 2408547 (2024).
- <sup>34</sup>E. Luchinat, L. Barbieri, M. Cremonini, A. Nocentini, C. T. Supuran, and L.  
Banci, *Angew. Chem.* **132**, 6597 (2020).